Published in Magnetic Resonance in Medicine (MRM):

DOI: 10.1002/mrm.27509

Prospective motion correction improves high-resolution quantitative susceptibility mapping (QSM) at 7 Tesla

Hendrik Mattern[1]*, Alessandro Sciarra[1], Falk Lüsebrink[1], Julio Acosta-Cabronero[2,3#], and Oliver Speck[1,3,4,5#]

[1] Department of Biomedical Magnetic Resonance, Institute for Physics, Otto-von-Guericke-University, Leipziger Str. 44, H65, 39120, Magdeburg, Germany.
[2] Wellcome Centre for Human Neuroimaging, Institute of Neurology, University College London, 12 Queen Square London WC1N 3BG, United Kingdom
[3] German Center for Neurodegenerative Diseases, Leipziger Straße 44, H64, 39120, Magdeburg, Germany.
[4] Center for Behavioral Brain Sciences, Magdeburg, Germany.
[5] Leibniz Institute for Neurobiology, Brenneckestr. 6, 39118, Magdeburg, Germany.

[#] joint last authors

***Corresponding author:**

Hendrik Mattern, M.Sc.,

Department of Biomedical Magnetic Resonance, Otto-von-Guericke University Magdeburg

Leipziger Str. 44 (Haus 65), Magdeburg 39120 Germany

E-mail: hendrik.mattern@ovgu.de, Tel: +49 391 6117 123, Fax: +49 391 6117 115

Short running head: Prospective motion correction improves QSM at 7 T

Word Count: Abstract: 199 (max 250)

Manuscript: 4669 (max 5000)

Numbers: Figures: 10

Tables: 0

References: 55

Abstract:

Purpose: Recent literature has shown the potential of high-resolution quantitative susceptibility mapping (QSM) with ultra-high field MRI for imaging the anatomy, the vasculature, and investigating their magnetostatic properties. Higher spatial resolutions, however, translate to longer scans resulting, thus, in higher vulnerability to, and likelihood of, subject movement. We hereby propose a gradient-recalled echo sequence with prospective motion correction (PMC) to address such limitation.

Methods: Data from four subjects were acquired at 7 Tesla. The effect of small and large motion on QSM with and without PMC was assessed qualitatively and quantitatively. Full brain QSM and QSM-based venograms with up to 0.33 mm isotropic voxel size were reconstructed.

Results: With PMC, motion artifacts in QSM and QSM-based venograms were largely eliminated, enabling — in both large- and small-amplitude motion regimes — accurate depiction of the cortex, vasculature and other small anatomical structures that are often blurred as a result of head movement or indiscernible at lower image resolutions. Quantitative analyses demonstrated that uncorrected motion could bias regional susceptibility distributions, a trend that was greatly reduced with PMC.

Conclusion: Qualitatively, PMC prevented image degradation due to motion artifacts, providing highly detailed QSM images and venograms. Quantitatively, PMC increased the reproducibility of susceptibility measures.

Keywords: Image artifacts, High resolution, Vasculature, Basal ganglia, Venography, Ultra high field

Introduction

Quantitative susceptibility mapping (QSM) — a new magnetic resonance imaging (MRI) post-processed contrast mechanism — provides superb anatomical detail of human brain structure (1) as well as venous vasculature (2) and quantifiable information on tissue composition (3,4). To date, QSM has shown strong potential for detecting cerebral microbleeds after traumatic brain injury (5) and for characterizing glioblastomas (6) — reviewed elsewhere (7,8). In addition, QSM is revealing novel information in aging (9–12); in chronic disorders of the nervous system such as multiple sclerosis (13,14), Alzheimer's disease (15,16), Parkinson's disease (17,18), Huntington's disease (19) or motor neuron disease (20); and has been used successfully for monitoring therapeutic intervention in neurodegeneration with brain iron accumulation (21).

Such a range of applications stem from the para-/ferromagnetic properties of most transition metals and metalloids, and the diamagnetism of inorganic compounds and myelin lipids, all of which influence the local magnetic susceptibilities of biological tissue. Across brain parenchyma, iron is thought to be the primary contributor to QSM contrast differences (22–25), though strong diamagnetic calcifications (26) and contributions of white matter microstructure (27) can modulate — sometimes dominate — local susceptibilities.

In practice, QSM calculation requires solving the inverse magnetostatic problem of inferring magnetic susceptibility sources from the local contributions to the field induction measured by the signal phase of a gradient-recalled echo (GRE) MRI sequence. It is well established that susceptibility-related frequency differences scale linearly with field strength, whereas noise in the GRE phase scales inversely proportional to the signal magnitude (28). Therefore, QSM benefits from the increased signal-to-noise ratio (SNR) capabilities of ultra-high field MRI (29), enabling higher image resolutions to study brain structures often indiscernible at clinical field strengths. This potential, however, is limited by subject motion. Involuntary, small-scale motion such as respiratory motion or slow head drifts are of the same order as the voxel size in high resolution imaging (30,31). Thus, small-scale motion can degrade the effective image resolution and can introduce spurious phase fluctuations as well as image shifts that generate inconsistencies between the measured field and the magnetostatic principles governing the susceptibility inversion procedure (32). Predictably, imperfect magnetic dipole deconvolution approaches — known to e.g. propagate streaking artifacts and amplify errors (33) — are further impaired by phase contamination due to motion; a scenario that can lead to severely corrupted QSM reconstructions

from high resolution GRE scans.

This study sets out to demonstrate the potential of prospective motion correction for in vivo QSM applications requiring very high image resolution. To that end, we developed a GRE pulse sequence with prospective motion correction functionality at 7 Tesla (7 T), reconstructed QSM and QSM-based venograms with up to 0.33 mm isotropic voxel size, and compared corrected and uncorrected data qualitatively and quantitatively for several motion amplitudes.

Methods

Subjects

Four cooperative healthy subjects (30±4 years old; one female) consented to participate in the study, which was approved by the local ethics committee. Subjects were retrospectively labeled based on the level of rotational motion observed during uncorrected scans (see Supporting Information Tab.S1), from low (subject #1) to high (subject #4).

Imaging Protocol

Experiments were performed on a 7 Tesla whole-body MRI system (Siemens Healthineers, Erlangen, Germany) using a quadrature transmit and 32-channel receive head coil (Nova Medical, Wilmington, Massachusetts, USA).

Pillows were placed in between head and coil to increase inter-subject positioning reproducibility and minimize motion. If not mentioned otherwise, all subjects were instructed to remain stationary to study the effect of unintentional motion. As a convention in this study, motion approximately on the order of the voxel size was considered to be small.

All subjects were scanned with an spoiled, fully flow-compensated, fully sampled, high-resolution 3D GRE sequence with prospective motion correction functionality using the following parameters: repetition time (TR)/ echo time (TE): 20/9.09ms; 10-degree flip angle; 200x166x110 mm^3 field of view; 0.33x0.33x1.25 mm^3 voxel resolution; and receiver bandwidth set to 120 Hz/pixel. Magnitude and phase images from each coil element were saved individually. The scan duration was 17:30 min. Each scan was performed with and without motion correction enabled (randomized order), with motion trajectories recorded for all scans. When enabled, motion was corrected prospectively for each k-space line. In order to assess the impact of larger motion on QSM, motion-

corrected and uncorrected scans for subject #3 were repeated with the instruction to change head orientation repeatedly during acquisition (alternating between periods of transitions to a new position and periods of rest). As an additional note, in this study a TE of 9 ms was empirically selected to provide sufficient susceptibility weighting while enabling shorter TR, hence, decreased overall scan durations.

To reconstruct QSM at 0.33 mm isotropic voxel size, subject #3 was additionally scanned with a high resolution protocol with the following modifications: 200x166x148 mm^3 field of view, receiver bandwidth set to 130 Hz/pixel, 6/8 partial Fourier in both phase encoding directions, two averages, scan duration 1:25 h. In order to improve signal-to-noise ratio (SNR) further, the high-resolution (two average) protocol was repeated twice (on different days) resulting, thus, in a total of four averages, i.e. approximately 3 h total scan time. Each scan was reconstructed separately, and then all were co-registered using ANTs v2.1 (34) ('antsRegistrationSyN.sh' performing rigid, affine, and deformable SyN registration in a multi-resolution routine).

In order to resolve independently the underlying anatomy, a high-resolution, motion-corrected, 3D magnetization-prepared rapid gradient echo (MPRAGE) sequence (35) was acquired for subject #3 with the following parameters: TR/ inversion time/TE: 2820/1050/2.82 ms; 5-degree flip angle; 225x225x187.2 mm^3 field of view; isotropic 0.45-mm isotropic voxel size; and receiver bandwidth set to 170 Hz/pixel. GRAPPA (36) was enabled with acceleration factor 2 and 24 reference lines, and 6/8 slice partial Fourier; resulting in a total scan time of 12:11 min.

Prospective motion correction

In order to correct for rigid-body motion and to prevent motion artifacts prospectively, a camera was used to track a marker attached to the subject's head. This enabled real-time updates of the imaging volume position and orientation, hence keeping a constant relationship between head and imaging volume. In brief, the tracking system (Metria Innovation, Milwaukee, Wisconsin, USA) consisted of an MR-compatible camera, a marker and a tracking computer. The camera was mounted with Velcro tape inside the MR bore above the subject's head. A single marker (15x15 mm^2) with Moiré phase patterns was attached to the subject via a custom mouth-piece based on dental impressions. Such set-up was found to provide the highest coupling between the marker and the subject's head, hence preventing false imaging volume updates (37). The camera tracked the marker with 0.01-mm and 0.01-degree precision (38). From the camera video stream — acquired at 80 frames per second — the tracking data was extracted and then sent to the MRI scanner to update the imaging volume every k-space line prior to the RF-excitation pulse with the most recent subject position and orientation. Even though this PMC approach requires external

hardware, it acquires tracking information independent of the MR acquisition. Therefore, the prescribed GRE protocol, which had virtually no dead time, had identical sequence timing for motion corrected and uncorrected cases, hence preventing longer scan durations or altering the steady state due to additional navigator scans. Further details on the motion correction system can be found elsewhere (31,38).

QSM reconstruction

The QSM reconstruction (summarized in Fig. 1) was optimized to preserve small structures in quantitative susceptibility maps and consisted of the following steps: first, a standard root-sum-of-squares combined magnitude image was generated to determine a BET2 (provided by FSL) (39) brain mask using a lenient fractional threshold of 0.1. Subsequently, unwrapped, background-filtered, offset-normalized single channel phases were obtained with HARPERELLA (40) – an iterative method (41) based on the spherical mean value (SMV) property (3) and the superposition principle of phase Laplacians. The radius of the convolving sphere used to calculate the Laplacian outside the field of view — which also defined the thickness of the brain boundary region — was 10 mm. To minimize aliasing errors and improve numerical accuracy, the field of view was enlarged in all three dimensions by 100, 100 and 50 pixels, respectively, setting those to zero (zero padding). Subsequently, 200 iterations were computed to approximate the phase Laplacian outside the brain-boundary region. Although channel-wise pre-processing can be time-consuming if not optimally implemented (e.g. single-threaded), an advantage of this method is that it accurately normalizes channel-specific phase offsets, yielding magnitude-weighted linear phase combinations with no singularity errors – a perennial problem in complex data combination of high-resolution data or when SNR is low (8,42). Locally-sourced inductions were subsequently revealed through further extraction of harmonic phases within the brain mask by SMV filtering with spatially varying spherical kernels (43); SMV kernel radius ranging from 25 mm at the center of the brain to 1 mm at boundary of the brain, without further deconvolution. Finally, the ℓ_1-norm penalty-based, morphology-enabled, non-linear dipole inversion (nMEDI) method (available from (44)) was used with dynamic model error reduction (MERIT) enabled and Lagrange multiplier set empirically to 1,000 (45).

Venogram calculation

Supporting Information Fig. S1 illustrates the intermediate steps devised for calculating QSM-based venograms from high-resolution phase data. The non-venous contributions to local field inductions were suppressed by the variable SMV approach using a starting radius of 3 mm (high-

pass frequency filtering), which was followed by the same nMEDI processing. Using small radii for SMV suppresses low spatial frequencies, thus, enhancing small structures such as the vasculature (see high-pass field in Supporting Information Fig. S1). The slice thickness of the high-pass filtered susceptibility maps (high-pass QSM) was up-sampled by b-spline interpolation to improve vessel continuity (resulting in nominal 0.33 mm isotropic voxel resolution). Unlike for susceptibility-weighted imaging, veins return high QSM values; thus, QSM-based venograms were calculated as maximum QSM projections over 60 slices (19.80 mm).

The same approach was used to calculate QSM-based venograms from the 0.33 mm dataset, except no up-sampling was applied and maximum QSM projections were computed over 45 slices (14.85 mm).

Extraction of regional susceptibility values

Susceptibility values were extracted for all subjects in the following regions of interest (ROIs): globus pallidus, caudate nucleus, putamen, thalamus, hippocampus, prefrontal gray matter (GM), and prefrontal white matter (WM). All ROIs were segmented bilaterally and were merged together for mean ± standard deviation calculation. Susceptibility values were referenced to the mean susceptibility value of cerebrospinal fluid (CSF), manually segmented from the frontal horns of the lateral ventricles (bilaterally).

ROI segmentation was performed on subject #3's T1-weighted MPRAGE dataset (see Supporting Information Fig. S2). After co-registration of all GRE magnitude images to MPRAGE space, inverse spatial transformations were applied to each ROI to generate masks in each native GRE-data space. Segmentation and co-registration methodologies are described in greater detail in Appendix A.

Statistical analysis

Recorded tracking data were used to calculate summary statistics (mean ± standard deviation) of 3D translational and rotational motion for each scan. Subsequently, differences in subject motion between PMC on and off were assessed separately for mean translation and rotation with non-parametric, two-sided, paired Wilcoxon signed-rank tests.

Paired Wilcoxon signed-rank tests were also utilized to assess whether regional mean susceptibilities differed between motion-corrected and uncorrected scans. For each subject individually, mean susceptibilities across all seven ROIs with motion correction were compared

with mean susceptibilities without motion correction under the null hypothesis that the difference between PMC on and PMC off came from a distribution with zero median.

Non-parametric, two-sample Kolmogorov-Smirnov (KS) test statistics reflect differences between two cumulative distribution functions. The effect of motion on QSM was analyzed for subject #3 through computation of KS test statistics for susceptibility distributions in each ROI. The following conditions were evaluated: (i) PMC on, unintentional motion (On/UnMo) versus PMC on, intentional motion (On/InMo); (ii) PMC off, unintentional motion (Off/UnMo) versus PMC off, intentional motion (Off/InMo). This intra-subject comparison was set out to assess whether data from unintentional, smaller motion and data from intentional, larger motion came from the same distribution (null-hypothesis). We hypothesized that, independent of motion amplitude, motion-corrected data would appear as if they were drawn from the same susceptibility distribution, whereas uncorrected susceptibility distributions from different motion regimes would differ. Additionally, KS tests were performed globally for whole-brain susceptibility distributions on both test conditions.

Furthermore, differences between motion-corrected and uncorrected data were quantitatively analyzed in an inter-subject comparison. For each subject, the impact of motion on QSM was assessed with ROI-wise KS tests on the null-hypothesis that motion-corrected and uncorrected susceptibility extractions (both from unintentional-motion scans) came from the same distribution. Associated *P*-values for all KS tests were Bonferroni adjusted (n=42, six test conditions × seven ROIs) for multiple-testing correction. Finally, whole-brain susceptibility distributions (PMC on versus PMC off) were assessed separately for each subject with KS tests.

All statistical tests were performed in MATLAB2015b (The MathWorks, Natick, Massachusetts, USA).

Results

Summary statistics for subject motion estimates and regional susceptibility extractions are reported in Supporting Information Tab. S1 and Supporting Information Tab. S2, respectively. Subject #3 was scanned with and without intentional motion to characterize the effect of motion on QSM both for corrected and uncorrected data. The comparison PMC on versus PMC off was performed using regional susceptibility data (across all subjects) in presence of unintentional motion.

Intra-subject: Effect of motion amplitude on corrected and uncorrected QSM

Subject #3 was scanned: (i) with motion correction during unintentional motion (On/UnMo), (ii) with correction during intentional motion (On/InMo), (iii) without correction during unintentional motion (Off/UnMo), and (iv) without correction during intentional motion (Off/InMo). Visual inspection of magnitude images (see Supporting Information Fig. S3), field maps (see Supporting Information Fig. S4), local field (see Supporting Information Fig. S5), QSM images (see Fig. 2), and venograms (see Fig. 3) suggest that motion artifacts—such as image blurring, ringing, and signal dropouts—are present at all stages of the QSM reconstruction pipeline; notably though, these were largely absent for prospectively motion-corrected data.

Data from unintentional motion was compared quantitatively to intentional motion both with and without PMC. Both Wilcoxon signed-rank tests (On/UnMo vs. On/InMo, $P = 0.69$, signed-rank=11; and Off/UnMo vs. Off/InMo, $P = 0.22$, signed-rank=6) were non-significant. Results for ROI-wise KS tests are shown in Fig. 4. KS test statistics appeared to be systematically lower for On/UnMo vs. On/InMo than for Off/UnMo vs. Off/InMo across all ROIs. With PMC disabled (off), all KS tests rejected the null hypothesis at $P_{Bonferroni} = 1*10^{-12}$. Applying the same threshold level, KS test differences with PMC on were only identified in two regions (prefrontal WM and thalamus); statistical differences were also observed in the corpus striatum, whereas QSM distributions from hippocampus and prefrontal grey matter ROIs were relatively unchanged across intentionally and unintentionally motion-corrupted scans with PMC enabled (on). KS test statistics for the whole brain were 0.005 (On/UnMo vs. On/InMo) and 0.050 (Off/UnMo vs. Off/InMo), respectively, i.e. an order of magnitude test-statistic increase when PMC was turned off.

Inter-subject: Comparison between motion-corrected and uncorrected QSM

Even when instructed to remain stationary, all healthy, young subjects moved considerably during the MRI acquisitions due to slow head drifts and physiological motion such as breathing (see Supporting Information Tab. S1). The mean 3D translation and rotation across scans were 1.42 mm and 0.42 degrees, respectively, which exceeded voxel dimensions. Although individual subjects motion estimates differed considerably between corrected and uncorrected scans, paired Wilcoxon signed-rank tests returned no significant differences in mean translation and rotation between PMC on and off across all subjects ($P = 0.88$).

On visual inspection, QSM (see Fig. 5) and QSM-based venograms (see Fig. 6) for all subjects demonstrated severe blurring due to motion in structures such as the highly paramagnetic venous vasculature; this is most apparent for larger motion (e.g. subject #4 in Fig. 6g and Fig. 6h), but it

is also noticeable for smaller motion (e.g. subject #1 and #2 in Fig. 6). PMC improved venous vessel depiction in three out of four cases (similar image quality was observed between PMC on and off for subject #3). The impact of small motion is less apparent on visual perception for QSM (see Fig. 5). Large movements induced visually traceable artifacts that degraded QSM reconstructions (see subject #4 in Fig. 5g and Fig. 5h), which was noticeably improved when using PMC. Importantly, regardless of motion level, PMC was never seen to degrade reconstruction quality compared to uncorrected data of similar motion.

In order to compare motion-corrected versus uncorrected data separately for each subject, Wilcoxon signed-rank tests for regional mean susceptibilities and KS tests for whole-brain distributions were performed (see Supporting Information Tab. S3). For greater motion (subject #4), regional mean susceptibilities differed significantly (P = 0.031; signed-rank=1). Consistent with this, subject #4 also returned the largest KS-test statistic. Additionally, regional susceptibility distributions between motion-corrected and uncorrected scans were also analyzed with KS-tests (see Fig. 7). In six out of seven cases, the subject with the largest motion (subject #4) resulted in the largest KS test statistic (all $P_{Bonferroni} < 1*10^{-12}$), whereas the subject with the smallest observed motion (subject #1) returned the smallest KS-test statistic in three out of seven cases. Computing the mean KS-test statistic across all ROIs for each subject showed that for subject #1 the average KS-test statistic (0.022) is approximately two times smaller than that for subject #2 (0.049) and subject #3 (0.042), and over four times smaller than that for subject #4 (0.099).

QSM at 0.33 mm isotropic voxel resolution

PMC was used to acquire QSM at 0.33 mm isotropic voxel size for a single subject. To ensure sufficient SNR the subject was scanned twice (on different days; scan time per session approximately 1.5 h). The subject moved 1.20±0.66 mm/0.42±0.22 degrees during session #1 and 4.93±1.26 mm/1.73±0.44 degrees during session #2. Overall motion in session #2 was approximately four times greater, demonstrating the unpredictable nature of head motion even when scanning the same healthy subject.

PMC enabled highly detailed QSM reconstructions accurately depicting small brain nuclei and thin structures commonly not visible at lower resolutions or blurred by uncorrected motion artifacts. Magnified axial and coronal views of corpus striatum/diencephalic regions in Fig. 8, for example, clearly depicted thalamic substructures such as the habenula (green arrows, Fig. 8a and Fig. 8b), anterior thalamic nucleus (blue arrows, Fig. 8d, Fig. 8l, and Fig. 8m) and mammillothalamic tracts (yellow arrows, Fig. 8). Furthermore, bilateral pockets of low paramagnetism could be readily identified in the caudal substantia nigra (pink arrows, Fig. 8e-g and Fig. 8k) – a subregion

commonly designated as substantia nigra nigrosome 1 (46). The substantia nigra ventral surface, the subthalamic nucleus, mammillary bodies and substructures of the red nucleus could also be clearly discerned on motion-corrected QSM. The cortical ribbon is also a relatively thin brain structure. As such, it greatly benefited from motion correction as illustrated in magnified axial views (see Fig. 9), where differential QSM patterns could be readily identified across the cortex. Thin hypointense structures between grey and white matter can be found across the cortex (yellow arrows). Also, diffused hyperintensities most prominent in adjacent white mattern, co-localized with the U-fiber layer, are marked with red arrows. These hyperintense patterns can also be seen in sagital views of occipital and temporal lobes in Supporting Information Fig. S6. Additionally, the hippocampus (note its digitations) is also accurately depicted (yellow arrows, Supporting Information Fig. S6). PMC also enabled detailed depiction of the venous vasculature as seen in axial, coronal, and sagittal views in Fig. 10. For example, the vascularization of the striatum and thalamus is clearly depicted in Fig. 10a; venous structures in the brainstem are also clearly identifiable in Fig. 10c.

Discussion

In this study, a spoiled GRE sequence with PMC functionality was combined with QSM reconstruction to compute high resolution susceptibility maps at ultra-high field. The reduction of motion artifacts with PMC improved QSM reconstruction for large and small motion both qualitatively and quantitatively. This enabled in vivo mapping of human brain macroscopic susceptibilities with up to 0.33 mm isotropic voxel resolution.

The present study showed that even young, healthy volunteers—who participate regularly in MRI research and were instructed to remain stationary—moved involuntarily due to slow head drifts and breathing (Supporting Information Tab. S1). Although this small, MR-experienced cohort moved on average less than 2 mm and 1 degree per scan, motion-induced qualitative and quantitative changes could be observed, which scaled to some extent as a function of motion amplitude (further discussed below). When imaging older subjects or neurodegenerative disease patients—highly relevant study groups for QSM—discomfort or anxiety could further increase subject motion. Therefore, motion and its correction for MR-naïve cohorts could be expected to have an even greater impact.

Visual inspections

From a qualitative standpoint, intra-subject and inter-subject comparisons showed that uncorrected, large-amplitude motion degraded QSM considerably (see Fig. 2d and Fig. 5h), leading to virtual loss of small-scale structures such as the venous vasculature (see Fig. 3d and Fig. 6h). PMC clearly reduced the impact of motion (see Fig. 2c, Fig. 3c, Fig. 5g, and Fig. 6g), however, minor residual errors can occur (discussed below). In the presence of small motion, e.g. respiratory motion (31) or slow head drifts (30), artifacts are less obvious on QSM, though depiction of small structures such as e.g. pial veins in prefrontal regions were considerably improved with PMC (see Fig. 6). Thus, in line with a recent MR angiography study (47), these results also highlight the benefits of high resolution and PMC on MR venography.

Quantitative study

For intra-subject as well as for inter-subject comparisons, our quantitative analyses were concordant with qualitative observations. We found evidence that larger motion can introduce significant errors in regional susceptibility extractions, which was confirmed by histogram analysis (see Fig. 4 for intra-subject and Fig 7 for inter-subject comparison). We observed an apparent correlation between motion amplitudes and KS-test statistics both for whole-brain and regional susceptibility distributions (see Fig. 7). Changes in regional susceptibility did not appear to be greater in the cortex than in deep gray matter. Importantly, when comparing data corrupted by intentional motion with data corrupted by unintentional motion (subject #3), we observed a systematic reduction in KS-test statistics when motion correction was applied (see Fig. 4). Thus, we can conclude for this single subject that independent of motion regime, the use of PMC results in more reproducible susceptibility distributions. Additionally, since the impact of motion corruption increases with spatial resolution, one might predict that the benefits of PMC would be further enhanced when imaging at spatial resolutions higher than $0.33\times0.33\times1.25$ mm^3, i.e. <0.5-mm isotropic voxels.

High resolution QSM

Long scan durations and small voxel sizes render high resolution MRI vulnerable to small-scale subject motion. Thus, motion correction has been applied retrospectively to GRE with isotropic voxel sizes up to 0.35-mm (48), and prospectively to MPRAGE up to 0.25-mm (49) and 0.15-mm time-of-flight angiography (47). In this study, QSM from GRE data with 0.33 mm isotropic voxel size was reconstructed. Compared to uncorrected QSMs with 0.40-mm isotropic resolution (1), this corresponds to approximately 1.8-fold decrease in voxel volume. At this spatial resolution, detailed depiction of small brain structures (such as digitations of the hippocampus, habenula and anterior thalamic nucleus, substantia nigra nigrosome 1, and venous vascularization) were

obtained (see Fig. 8, Supporting Information Fig. S6, and Fig. 10). This is relevant in that, for example, reliable QSM measurements of the nigrosome 1 might enable early detection of neurodegenerative processes and monitoring of therapeutic impact in several movement disorders including Parkinson's disease (46,50,51). It is worth noting that QSM at such high resolution also enables the study of magnetostatic variations both across cortex and between cortex and subcortical white matter (see Fig 9. and Supporting Information Fig. S6). Other potential use cases for ultra-high resolution QSM are the study of vessel malformations, small vessel disease and improved microbleed detection; whereas motion-corrected venograms could be used e.g. to mask out draining vessels in GRE-based echo planar imaging for high-resolution functional MRI.

In conclusion, motion-corrected, high resolution QSM has great potential for investigating subtle aging and disease related susceptibility changes, including those in the vasculature. Future clinical studies are warranted to evaluate the feasibility and performance of PMC-QSM for such applications.

Limitations and future work

PMC updates position and orientation of the imaging volume but does not account for changes of the subject's head with respect to receiver profiles, or changes in orientation of the brain with respect to the magnetic field. The former can be addressed retrospectively (52). In addition, real-time field-control has been used to correct for spatiotemporal magnetic field fluctuations in QSM (53). Alternatively, navigators have also been successfully applied to correct for physiological field fluctuations (54). Since PMC cannot correct for changes in the magnetic field, however, potential residual field perturbation could have biased the present results. This is expected to be highly relevant if head motion changes the alignment between the anatomy and the static magnetic field, i.e. large through-plane rotations, though less impactful for small-scale translation. Therefore, future combinations of PMC technology with real-time field-control might hold great potential for acquiring QSM data free of any erroneous field perturbation.

A further limitation of this work is that with the use of PMC, uncorrected data for direct comparison is unavailable. Thus, scans were repeated (back-to-back) with and without motion correction enabled, the latter to approximate uncorrected data. Although such an approach is widely accepted in this context (31,47), it is noteworthy that subject motion is not entirely reproducible. Additionally, statistical estimates neglect that motion during the acquisition of low k-space frequencies might have a greater impact on image quality than motion during the encoding of high frequencies. Due to these limitations and the limited cohort size in this study, simulating motion in

QSM would be an alternative approach which could provide (synthetic) uncorrected, corrected and ground-truth data. However, implementing realistic models is challenging.

A final point worth discussing is that rating motion qualitatively, e.g. small versus large, depends on study-specific definitions, which might differ considerably across studies. Developing a generalized, k-space-weighted motion metric was beyond the scope of the study but warrants a future investigation.

Conclusion

Subject motion impairs in vivo QSM by degrading the effective image resolution and introducing destructive signal interferences that impair the reconstruction. Prospective motion correction maximized the capabilities of ultra-high resolution QSM, enabling superb detail of subcortical structures, cortex and vasculature with up to 0.33 mm isotropic voxel size, and may lead to more reproducible QSM measurements in the presence of motion.

Acknowledgements

This work was supported by the National Institutes of Health, grant number 1R01-DA021146 and the Initial Training Network, HiMR, funded by the FP7 Marie Curie Actions of the European Commission, grant number FP7-PEOPLE-2012-ITN-316716. The Wellcome Centre for Human Neuroimaging is supported by core funding from the Wellcome Trust (203147/Z/16/Z). The authors would like to thank the staff of the Department of Oral and Maxillofacial Surgery, University Hospital Magdeburg A.ö.R. for creating the custom-built mouth pieces.

Appendix A: Segmentation and co-registration

To quantify regional susceptibility distributions, ROI segmentation was performed on subject #3's bias field corrected (using SPM12 (55)), T1-weighted MPRAGE dataset. Subcortical GM ROIs were segmented with FSL FIRST (56). Whole-brain GM, WM and CSF segments calculated with SPM were subsequently thresholded at probability = 0.9, binarized, and intersected separately with the manually traced prefrontal ROIs to generate tissue-specific masks. Masks were finally eroded by one voxel in 3D for GM and WM ROIs, by three voxels for caudate and CSF, and by

five voxels for all other ROIs; noting erosion strength was empirically optimized to prevent edge effects. Supporting Information Fig. S2 shows ROI masks overlaid onto subject #3's MPRAGE image.

The anatomical MPRAGE dataset from subject #3 was then co-registered to subject #3's average GRE magnitude template using ANTs v2.1 (34) ('antsRegistrationSyN.sh' performing rigid, affine, and deformable SyN registration). The GRE magnitude template was constructed iteratively applying the nonlinear 'antsMultivariateTemplateConstruction.sh' routine to subject #3's four GRE magnitude images. GRE scans from subject #1, #2, and #4 were subsequently co-registered to this template using 'antsRegistrationSyN.sh'. The composition of inverse transformations was applied to each ROI followed by nearest-neighbor interpolation to create ROI masks in each data space. This approach enabled extraction of regional susceptibility values in each individual QSM space (excluding potential numerical bias due to spatial interpolation).

References

1. Deistung A, Schäfer A, Schweser F, Biedermann U, Turner R, Reichenbach JR. Toward in vivo histology: A comparison of quantitative susceptibility mapping (QSM) with magnitude-, phase-, and R2*-imaging at ultra-high magnetic field strength. Neuroimage [Internet]. 2013;65:299–314 doi: 10.1016/j.neuroimage.2012.09.055.
2. Fan AP, Bilgic B, Gagnon L, Witzel T, Bhat H, Rosen BR, Adalsteinsson E. Quantitative oxygenation venography from MRI phase. Magn. Reson. Med. [Internet]. 2014;72(1):149–159 doi: 10.1002/mrm.24918.
3. Schweser F, Deistung A, Lehr BW, Reichenbach JR. Quantitative imaging of intrinsic magnetic tissue properties using MRI signal phase: an approach to in vivo brain iron metabolism? Neuroimage [Internet]. 2011;54(4):2789–2807. eng doi: 10.1016/j.neuroimage.2010.10.070.
4. Stuber C, Morawski M, Schafer A et al. Myelin and iron concentration in the human brain: a quantitative study of MRI contrast. Neuroimage [Internet]. 2014;93 Pt 1:95–106. eng doi: 10.1016/j.neuroimage.2014.02.026.
5. Liu J, Xia S, Hanks R, Wiseman N, Peng C, Zhou S, Haacke EM, Kou Z. Susceptibility Weighted Imaging and Mapping of Micro-Hemorrhages and Major Deep Veins after Traumatic Brain Injury. J Neurotrauma [Internet]. 2016;33(1):10–21. eng doi: 10.1089/neu.2014.3856.
6. Deistung A, Schweser F, Wiestler B et al. Quantitative susceptibility mapping differentiates between blood depositions and calcifications in patients with glioblastoma. PLoS ONE [Internet]. 2013;8(3):e57924. eng doi: 10.1371/journal.pone.0057924.
7. Reichenbach JR, Schweser F, Serres B, Deistung A. Quantitative Susceptibility Mapping: Concepts and Applications. Clin Neuroradiol [Internet]. 2015;25 Suppl 2:225–230. eng doi: 10.1007/s00062-015-0432-9.

8. Haacke EM, Liu S, Buch S, Zheng W, Wu D, Ye Y. Quantitative susceptibility mapping: current status and future directions. J Magn Reson Imaging [Internet]. 2015;33(1):1–25. eng doi: 10.1016/j.mri.2014.09.004.
9. Li W, Wu B, Batrachenko A et al. Differential developmental trajectories of magnetic susceptibility in human brain gray and white matter over the lifespan. Hum Brain Mapp [Internet]. 2014;35(6):2698–2713. eng doi: 10.1002/hbm.22360.
10. Persson N, Wu J, Zhang Q, Liu T, Shen J, Bao R, Ni M, Liu T, Wang Y, Spincemaille P. Age and sex related differences in subcortical brain iron concentrations among healthy adults. Neuroimage [Internet]. 2015;122:385–398. eng doi: 10.1016/j.neuroimage.2015.07.050.
11. Acosta-Cabronero J, Betts MJ, Cardenas-Blanco A, Yang S, Nestor PJ. In Vivo MRI Mapping of Brain Iron Deposition across the Adult Lifespan. J Neurosci [Internet]. 2016;36(2):364–374. eng doi: 10.1523/JNEUROSCI.1907-15.2016.
12. Betts MJ, Acosta-Cabronero J, Cardenas-Blanco A, Nestor PJ, Duzel E. High-resolution characterisation of the aging brain using simultaneous quantitative susceptibility mapping (QSM) and R* measurements at 7T. Neuroimage [Internet]. 2016. ENG doi: 10.1016/j.neuroimage.2016.05.024.
13. Langkammer C, Liu T, Khalil M, Enzinger C, Jehna M, Fuchs S, Fazekas F, Wang Y, Ropele S. Quantitative susceptibility mapping in multiple sclerosis. Radiology [Internet]. 2013;267(2):551–559. eng doi: 10.1148/radiol.12120707.
14. Wisnieff C, Ramanan S, Olesik J, Gauthier S, Wang Y, Pitt D. Quantitative susceptibility mapping (QSM) of white matter multiple sclerosis lesions: Interpreting positive susceptibility and the presence of iron. Magn Reson Med [Internet]. 2015;74(2):564–570. eng doi: 10.1002/mrm.25420.
15. Acosta-Cabronero J, Williams GB, Cardenas-Blanco A, Arnold RJ, Lupson V, Nestor PJ. In vivo quantitative susceptibility mapping (QSM) in Alzheimer's disease. PLoS ONE [Internet]. 2013;8(11):e81093. eng doi: 10.1371/journal.pone.0081093.
16. Moon Y, Han S-H, Moon W-J. Patterns of Brain Iron Accumulation in Vascular Dementia and Alzheimer's Dementia Using Quantitative Susceptibility Mapping Imaging. J Alzheimers Dis [Internet]. 2016;51(3):737–745. eng doi: 10.3233/JAD-151037.
17. He N, Ling H, Ding B, Huang J, Zhang Y, Zhang Z, Liu C, Chen K, Yan F. Region-specific disturbed iron distribution in early idiopathic Parkinson's disease measured by quantitative susceptibility mapping. Hum Brain Mapp [Internet]. 2015;36(11):4407–4420. eng doi: 10.1002/hbm.22928.
18. Guan X, Xuan M, Gu Q, Huang P, Liu C, Wang N, Xu X, Luo W, Zhang M. Regionally progressive accumulation of iron in Parkinson's disease as measured by quantitative susceptibility mapping. NMR Biomed [Internet]. 2016. ENG doi: 10.1002/nbm.3489.
19. van Bergen JMG, Hua J, Unschuld PG, Lim IAL, Jones CK, Margolis RL, Ross CA, van Zijl PCM, Li X. Quantitative Susceptibility Mapping Suggests Altered Brain Iron in Premanifest Huntington Disease. AJNR Am J Neuroradiol [Internet]. 2016;37(5):789–796. eng doi: 10.3174/ajnr.A4617.
20. Schweitzer AD, Liu T, Gupta A, Zheng K, Seedial S, Shtilbans A, Shahbazi M, Lange D, Wang Y, Tsiouris AJ. Quantitative susceptibility mapping of the motor cortex in amyotrophic lateral sclerosis and primary lateral sclerosis. AJR Am J Roentgenol [Internet]. 2015;204(5):1086–1092. eng doi: 10.2214/AJR.14.13459.

21. Lobel U, Schweser F, Nickel M et al. Brain iron quantification by MRI in mitochondrial membrane protein-associated neurodegeneration under iron-chelating therapy. Ann Clin Transl Neurol [Internet]. 2014;1(12):1041–1046. eng doi: 10.1002/acn3.116.
22. Fukunaga M, Li T-Q, van Gelderen P et al. Layer-specific variation of iron content in cerebral cortex as a source of MRI contrast. Proc Natl Acad Sci U S A [Internet]. 2010;107(8):3834–3839. eng doi: 10.1073/pnas.0911177107.
23. Langkammer C, Schweser F, Krebs N et al. Quantitative susceptibility mapping (QSM) as a means to measure brain iron? A post mortem validation study. Neuroimage [Internet]. 2012;62(3):1593–1599. eng doi: 10.1016/j.neuroimage.2012.05.049.
24. Sun H, Walsh AJ, Lebel RM, Blevins G, Catz I, Lu J-Q, Johnson ES, Emery DJ, Warren KG, Wilman AH. Validation of quantitative susceptibility mapping with Perls' iron staining for subcortical gray matter. Neuroimage [Internet]. 2015;105:486–492. eng doi: 10.1016/j.neuroimage.2014.11.010.
25. Zheng W, Nichol H, Liu S, Cheng Y-CN, Haacke EM. Measuring iron in the brain using quantitative susceptibility mapping and X-ray fluorescence imaging. Neuroimage [Internet]. 2013;78:68–74. eng doi: 10.1016/j.neuroimage.2013.04.022.
26. Schweser F, Deistung A, Lehr BW, Reichenbach JR. Differentiation between diamagnetic and paramagnetic cerebral lesions based on magnetic susceptibility mapping. Med Phys [Internet]. 2010;37(10):5165–5178. eng doi: 10.1118/1.3481505.
27. Wharton S, Bowtell R. Effects of white matter microstructure on phase and susceptibility maps. Magn Reson Med [Internet]. 2015;73(3):1258–1269. eng doi: 10.1002/mrm.25189.
28. Gudbjartsson H, Patz S. The rician distribution of noisy mri data. Magn. Reson. Med. [Internet]. 1995;34(6):910–914 doi: 10.1002/mrm.1910340618.
29. Pohmann R, Speck O, Scheffler K. Signal-to-noise ratio and MR tissue parameters in human brain imaging at 3, 7, and 9.4 tesla using current receive coil arrays. Magn Reson Med [Internet]. 2016;75(2):801–809. eng doi: 10.1002/mrm.25677.
30. Herbst M, Maclaren J, Lovell-Smith C, Sostheim R, Egger K, Harloff A, Korvink J, Hennig J, Zaitsev M. Reproduction of motion artifacts for performance analysis of prospective motion correction in MRI. Magn. Reson. Med. [Internet]. 2014;71(1):182–190 doi: 10.1002/mrm.24645.
31. Stucht D, Danishad KA, Schulze P, Godenschweger F, Zaitsev M, Speck O. Highest Resolution In Vivo Human Brain MRI Using Prospective Motion Correction. PLoS ONE [Internet]. 2015;10(7):e0133921. eng doi: 10.1371/journal.pone.0133921.
32. Deistung A, Schweser F, Reichenbach JR. Overview of quantitative susceptibility mapping. NMR Biomed [Internet]. 2016. ENG doi: 10.1002/nbm.3569.
33. Wang S, Liu T, Chen W, Spincemaille P, Wisnieff C, Tsiouris AJ, Zhu W, Pan C, Zhao L, Wang Y. Noise Effects in Various Quantitative Susceptibility Mapping Methods. IEEE Trans Biomed Eng [Internet]. 2013;60(12):3441–3448. eng doi: 10.1109/TBME.2013.2266795.
34. Avants B, Epstein C, Grossman M, Gee J. Symmetric diffeomorphic image registration with cross-correlation: Evaluating automated labeling of elderly and neurodegenerative brain. Medical Image Analysis [Internet]. 2008;12(1):26–41 doi: 10.1016/j.media.2007.06.004.
35. Mugler JP, Brookeman JR. Three-dimensional magnetization-prepared rapid gradient-echo imaging (3D MP RAGE). Magn. Reson. Med. [Internet]. 1990;15(1):152–157 doi: 10.1002/mrm.1910150117.

36. Griswold MA, Jakob PM, Heidemann RM, Nittka M, Jellus V, Wang J, Kiefer B, Haase A. Generalized autocalibrating partially parallel acquisitions (GRAPPA). Magn. Reson. Med. [Internet]. 2002;47(6):1202–1210 doi: 10.1002/mrm.10171.
37. Pannetier NA, Stavrinos T, Ng P, Herbst M, Zaitsev M, Young K, Matson G, Schuff N. Quantitative framework for prospective motion correction evaluation. Magn Reson Med [Internet]. 2016;75(2):810–816. eng doi: 10.1002/mrm.25580.
38. Maclaren J, Armstrong, Brian S R, Barrows RT et al. Measurement and correction of microscopic head motion during magnetic resonance imaging of the brain. PLoS ONE [Internet]. 2012;7(11):e48088. eng doi: 10.1371/journal.pone.0048088.
39. Smith SM. Fast robust automated brain extraction. Hum Brain Mapp [Internet]. 2002;17(3):143–155. eng doi: 10.1002/hbm.10062.
40. Li W, Avram AV, Wu B, Xiao X, Liu C. Integrated Laplacian-based phase unwrapping and background phase removal for quantitative susceptibility mapping. NMR Biomed [Internet]. 2014;27(2):219–227. eng doi: 10.1002/nbm.3056.
41. http://people.duke.edu/~cl160/. STI Suite [Internet]; 2013 [modified 2013 Aug 30; cited 2016 Jul 28]. Available from: http://people.duke.edu/~cl160/.
42. Robinson SD, Bredies K, Khabipova D, Dymerska B, Marques JP, Schweser F. An illustrated comparison of processing methods for MR phase imaging and QSM: Combining array coil signals and phase unwrapping. NMR Biomed [Internet]. 2017;30(4). eng doi: 10.1002/nbm.3601.
43. Li W, Wu B, Liu C. Quantitative susceptibility mapping of human brain reflects spatial variation in tissue composition. Neuroimage [Internet]. 2011;55(4):1645–1656. eng doi: 10.1016/j.neuroimage.2010.11.088.
44. http://weill.cornell.edu/mri/pages/qsm.html. Cornell QSM [Internet] [cited 2016 Jul 28]. Available from: http://weill.cornell.edu/mri/pages/qsm.html.
45. Liu T, Wisnieff C, Lou M, Chen W, Spincemaille P, Wang Y. Nonlinear formulation of the magnetic field to source relationship for robust quantitative susceptibility mapping. Magn Reson Med [Internet]. 2013;69(2):467–476. eng doi: 10.1002/mrm.24272.
46. Lehericy S, Bardinet E, Poupon C, Vidailhet M, Francois C. 7 Tesla magnetic resonance imaging: a closer look at substantia nigra anatomy in Parkinson's disease. Mov Disord [Internet]. 2014;29(13):1574–1581. eng doi: 10.1002/mds.26043.
47. Mattern H, Sciarra A, Godenschweger F, Stucht D, Lüsebrink F, Rose G, Speck O. Prospective motion correction enables highest resolution time-of-flight angiography at 7T. Magn Reson Med [Internet]. 2018;80(1):248–258. eng doi: 10.1002/mrm.27033.
48. Federau C, Gallichan D. Motion-Correction Enabled Ultra-High Resolution In-Vivo 7T-MRI of the Brain. PLoS ONE [Internet]. 2016;11(5):e0154974. ENG doi: 10.1371/journal.pone.0154974.
49. Lüsebrink F, Sciarra A, Mattern H, Yakupov R, Speck O. T1-weighted in vivo human whole brain MRI dataset with an ultrahigh isotropic resolution of 250 μm. Sci. Data [Internet]. 2017;4:170032 doi: 10.1038/sdata.2017.32.
50. Kwon D-H, Kim J-M, Oh S-H, Jeong H-J, Park S-Y, Oh E-S, Chi J-G, Kim Y-B, Jeon BS, Cho Z-H. Seven-Tesla magnetic resonance images of the substantia nigra in Parkinson disease. Ann Neurol [Internet]. 2012;71(2):267–277. eng doi: 10.1002/ana.22592.

51. Acosta-Cabronero J, Cardenas-Blanco A, Betts MJ, Butryn M, Valdes-Herrera JP, Galazky I, Nestor PJ. The whole-brain pattern of magnetic susceptibility perturbations in Parkinson's disease. Brain [Internet]. 2017;140(1):118–131. eng doi: 10.1093/brain/aww278.
52. Yarach U, Luengviriya C, Stucht D, Godenschweger F, Schulze P, Speck O. Correction of B 0-induced geometric distortion variations in prospective motion correction for 7T MRI. MAGMA [Internet]. 2016. eng doi: 10.1007/s10334-015-0515-2.
53. Özbay PS, Duerst Y, Wilm BJ, Pruessmann KP, Nanz D. Enhanced quantitative susceptibility mapping (QSM) using real-time field control. Magn Reson Med [Internet]. 2017. eng doi: 10.1002/mrm.26735.
54. Wen J, Cross AH, Yablonskiy DA. On the role of physiological fluctuations in quantitative gradient echo MRI: Implications for GEPCI, QSM, and SWI. Magn Reson Med [Internet]. 2015;73(1):195–203. eng doi: 10.1002/mrm.25114.
55. Friston KJ. Statistical parametric mapping: The analysis of functional brain images. London: Academic; 2007.
56. Patenaude B, Smith SM, Kennedy DN, Jenkinson M. A Bayesian model of shape and appearance for subcortical brain segmentation. Neuroimage [Internet]. 2011;56(3):907–922. eng doi: 10.1016/j.neuroimage.2011.02.046.

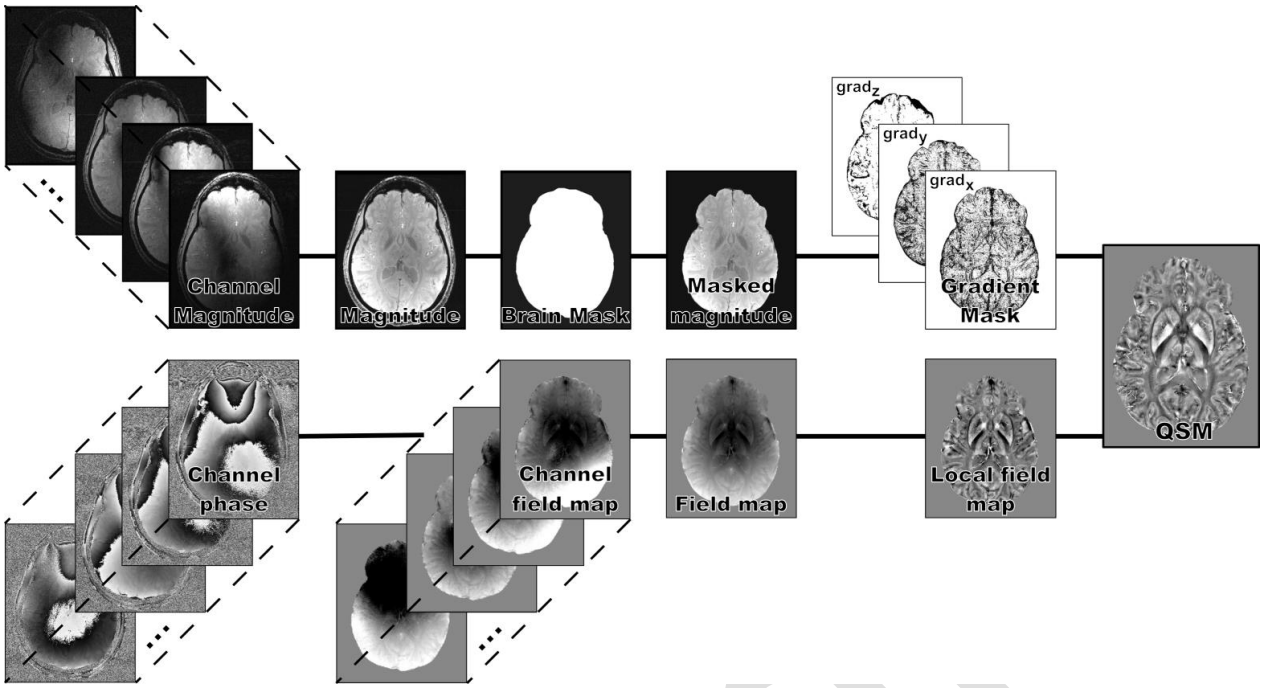

Figure 1: Proposed processing pipeline for QSM at ultra-high field. First, channel-wise magnitude images were combined with a standard root-sum-of-squares method to create a brain mask. Subsequently, the combined field map was inferred from magnitude-weighted, HARPERELLA-processed channel phases. Locally sourced inductions were subsequently revealed by SMV filtering with spatially varying spherical kernels. Finally, ℓ_1-norm based regularized QSM inversions were performed using the non-linear, morphology-enabled, dipole inversion (nMEDI) method.
QSM, quantitative susceptibility mapping; SMV, spherical mean value.

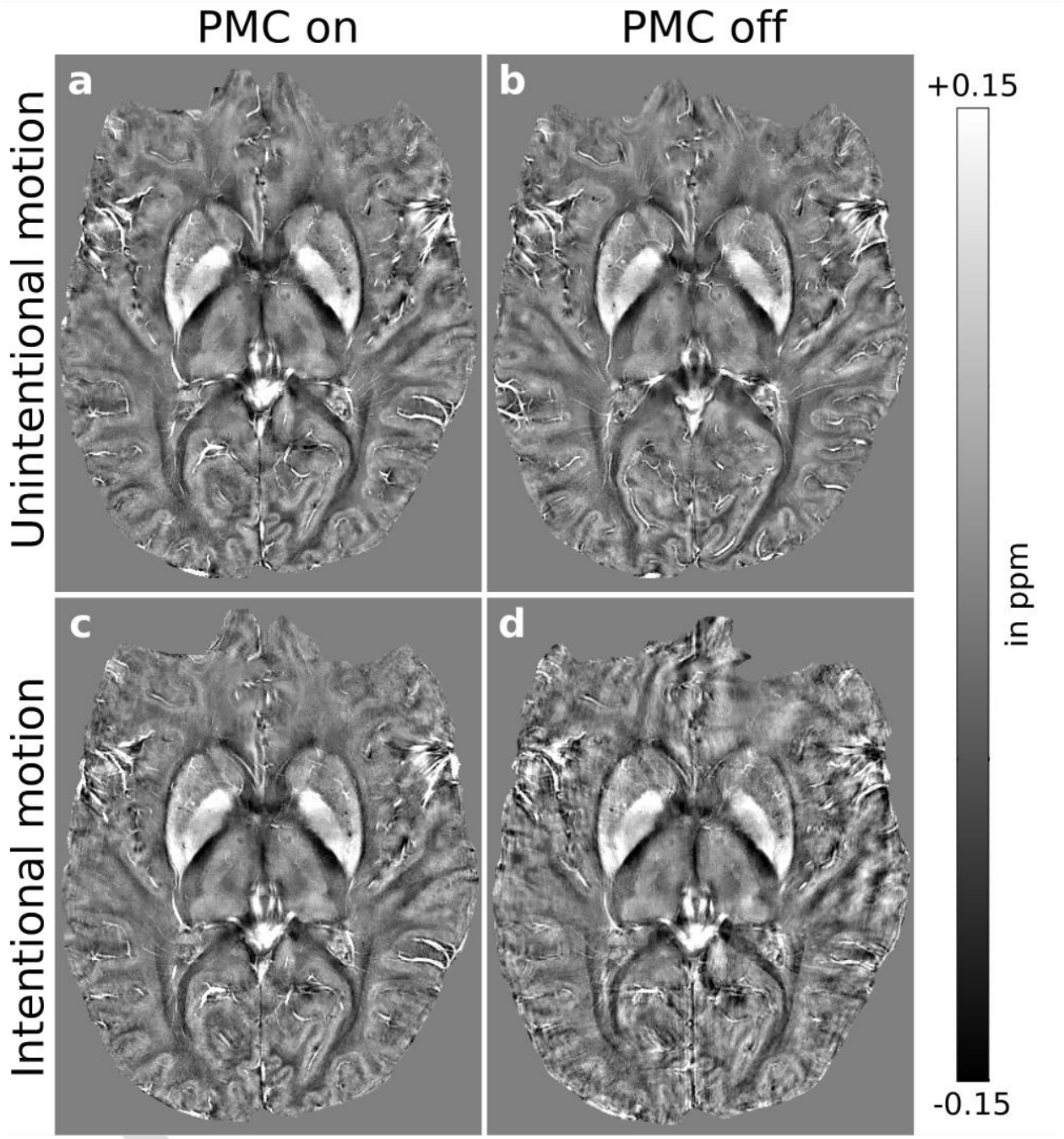

Figure 2: Intra-subject comparison (subject #3) of (a, c) motion-corrected and (b, d) uncorrected QSM, (a, b) without and (c, d) with intentional motion. For small-scale motion, corrected and uncorrected QSM showed no apparent motion artifacts. For large-scale motion, uncorrected maps were degraded; this effect was reduced with motion correction leading to minor residual artifacts.
QSM, quantitative susceptibility mapping.

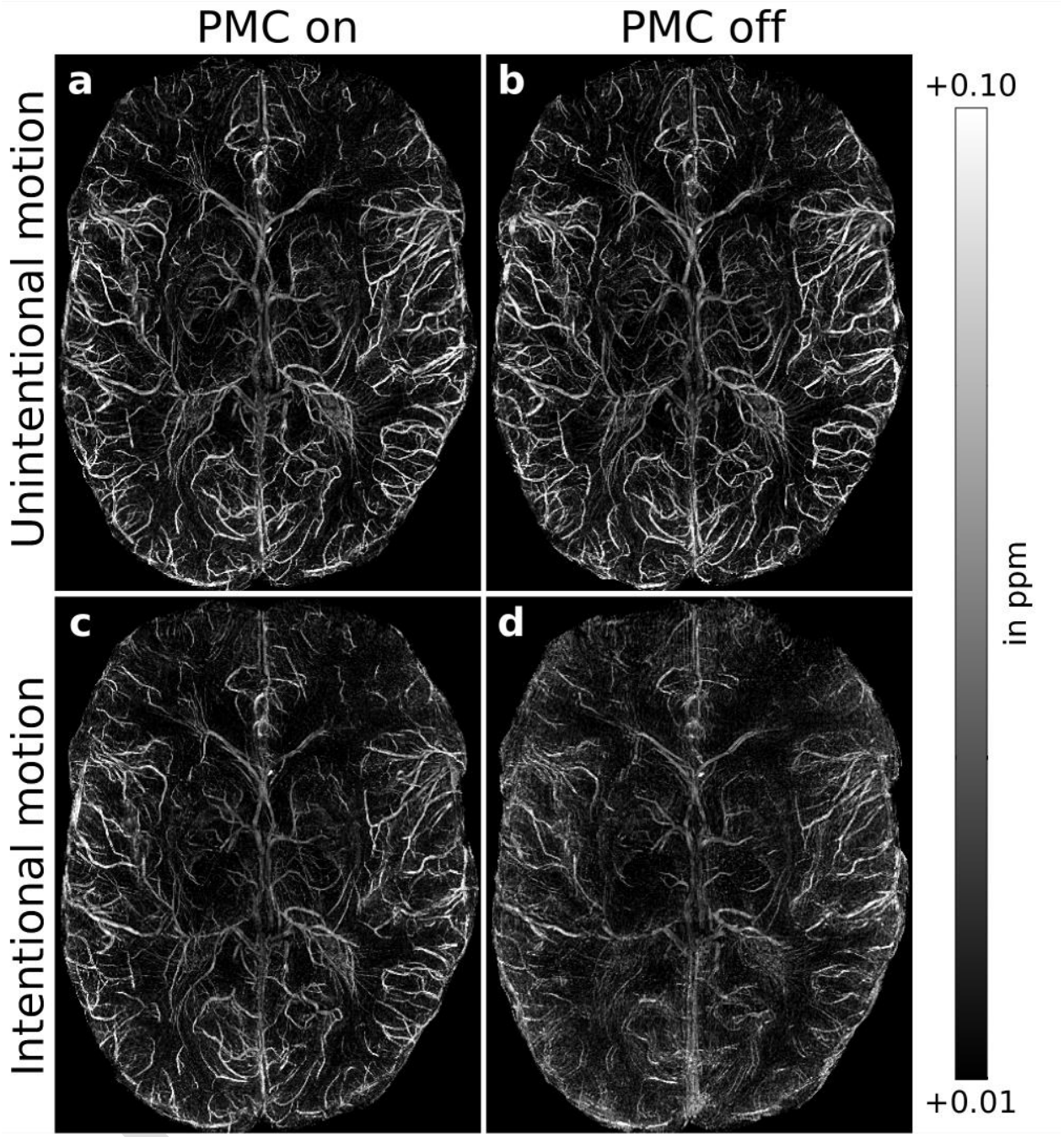

Figure 3: Intra-subject comparison (subject #3) of (a, c) motion-corrected and (b, d) uncorrected QSM-based venograms, (a, b) without and (c, d) with intentional motion. For small-scale motion, corrected and uncorrected QSM showed no apparent motion artifacts. Without correction, large-scale motion degraded vessel depiction considerably; this effect was largely prevented by motion correction leading to minor residual artifacts.
QSM, quantitative susceptibility mapping.

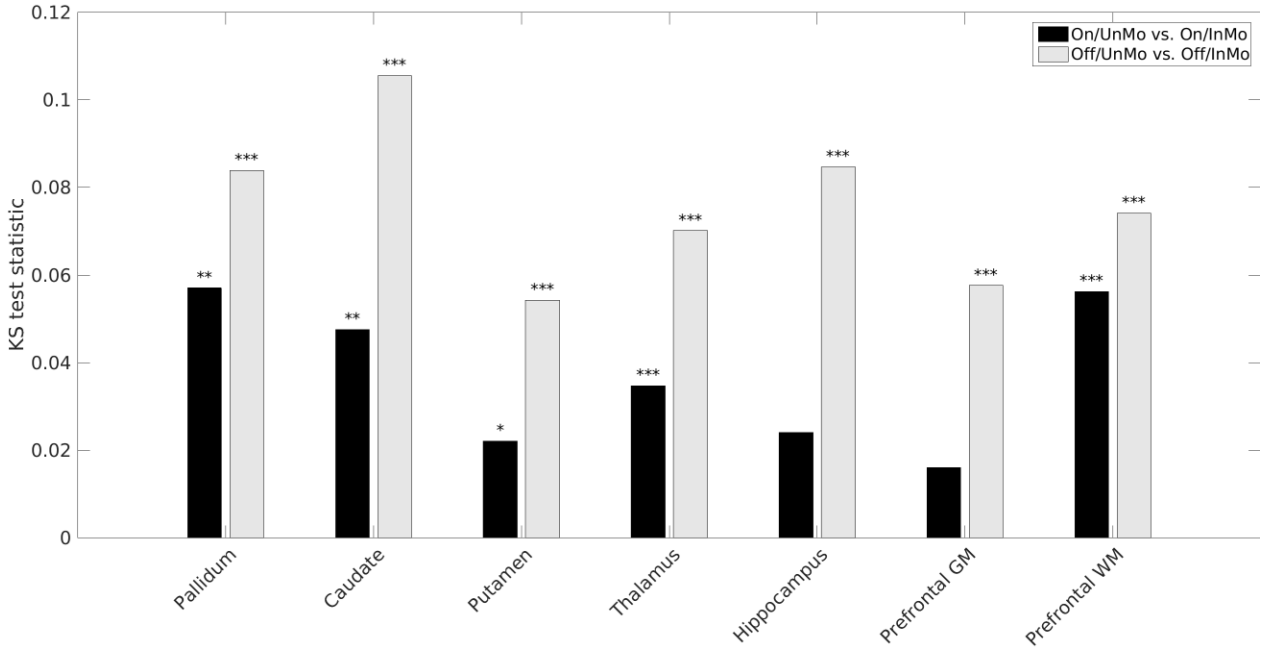

*Figure 4: Intra-subject evaluation of regional QSM distributions using KS tests. Condition 1: PMC on, unintentional motion (On/UnMo) vs. PMC on, intentional motion (On/InMo); Condition 2: PMC off, unintentional motion (Off/UnMo) vs. PMC off, intentional motion (Off/InMo). Statistical significance denoted as * $P_{Bonferroni}$ <0.01, ** $P_{Bonferroni}$ <1*10^{-6}, and *** $P_{Bonferroni}$ <1*10^{-12}. Systematically lower KS test statistics were obtained for motion-corrected data.*
QSM, Quantitative Susceptibility Mapping; KS, Kolmogorov-Smirnov; PMC, Prospective Motion Correction; GM, gray mattern; WM, white matter.

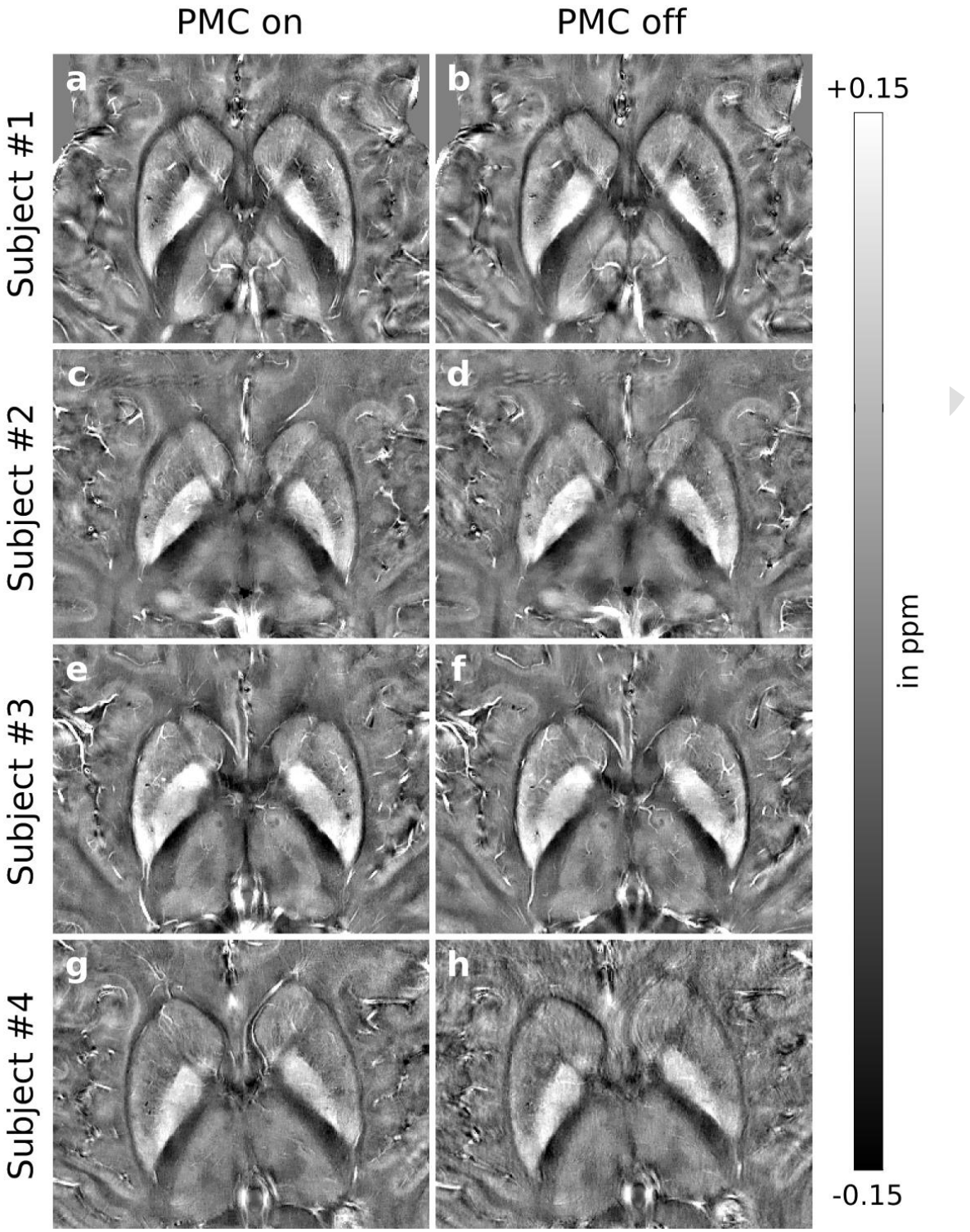

Figure 5: Inter-subject comparison of (a, c, e, g) motion-corrected and (b, d, f, h) uncorrected QSM. Smaller motion did not visibly degrade QSM reconstructions, whereas larger, uncorrected motion corrupted QSM. With motion correction, QSM degradation was successfully reduced in two of four subjects. For the remaining two subjects, image quality was similar with PMC on and PMC off.

PMC, Prospective Motion Correction; QSM, Quantitative Susceptibility Mapping.

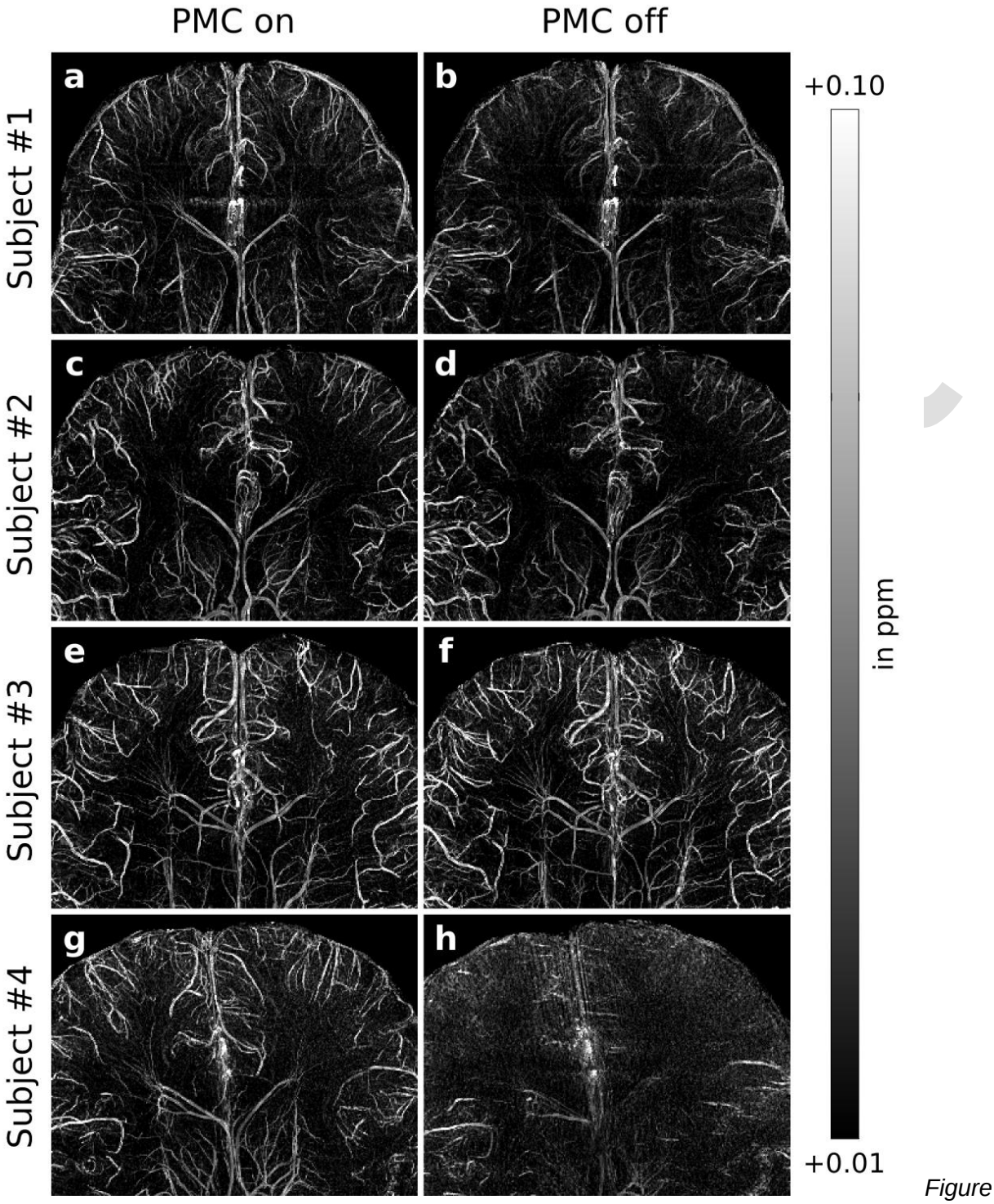

Figure 6: Inter-subject comparison of (a, c, e, g) motion-corrected and (b, d, f, h) uncorrected QSM-based venograms. Larger, uncorrected motion corrupted the venograms. Smaller motion (on the order of the voxel dimension) also blurred vessels — particularly across prefrontal areas (shown here). Sharper and more detailed venograms were obtained in both motion regimes with motion correction in three of four subjects. For subject #3, image quality was similar with PMC on and PMC off.

PMC, Prospective Motion Correction; QSM, Quantitative Susceptibility Mapping.

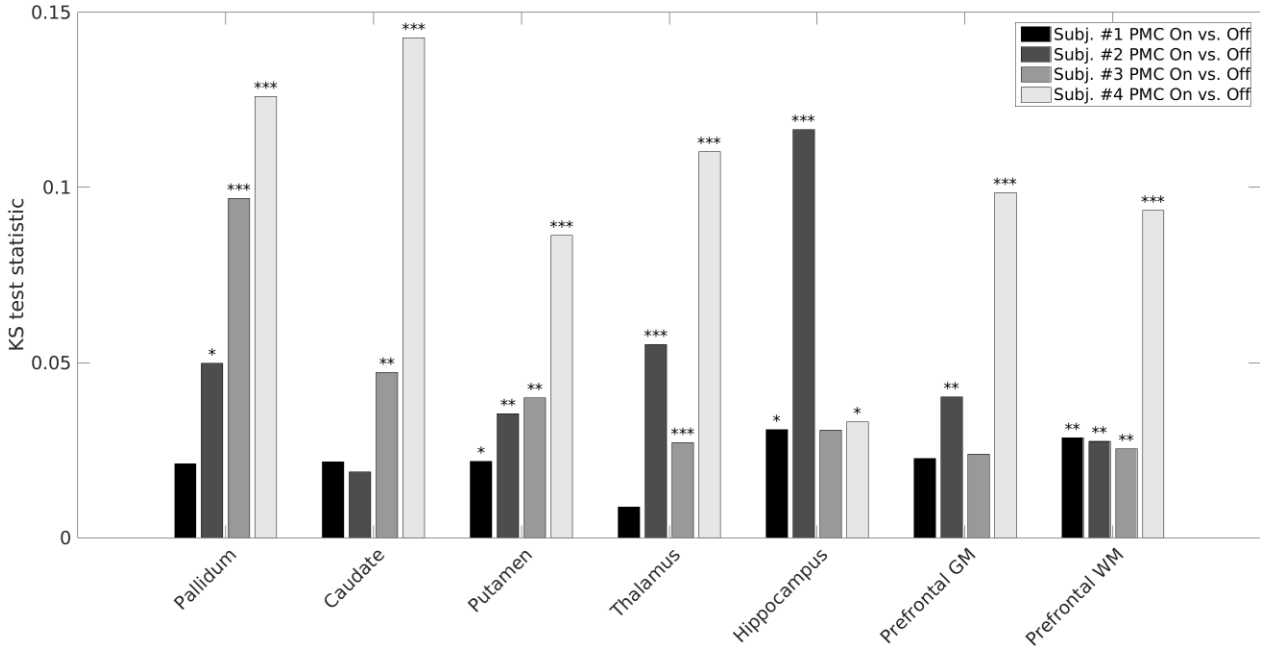

*Figure 7: Individual KS test results comparing regional QSM distributions from motion-corrected vs. uncorrected data. Statistical significance denoted as * $P_{Bonferroni}$ <0.01, ** $P_{Bonferroni}$ <1*10^{-6}, and *** $P_{Bonferroni}$ <1*10^{-12}.*
PMC, Prospective Motion Correction; QSM, Quantitative Susceptibility Mapping; KS, Kolmogorov-Smirnov; GM, gray matter; WM, white matter.

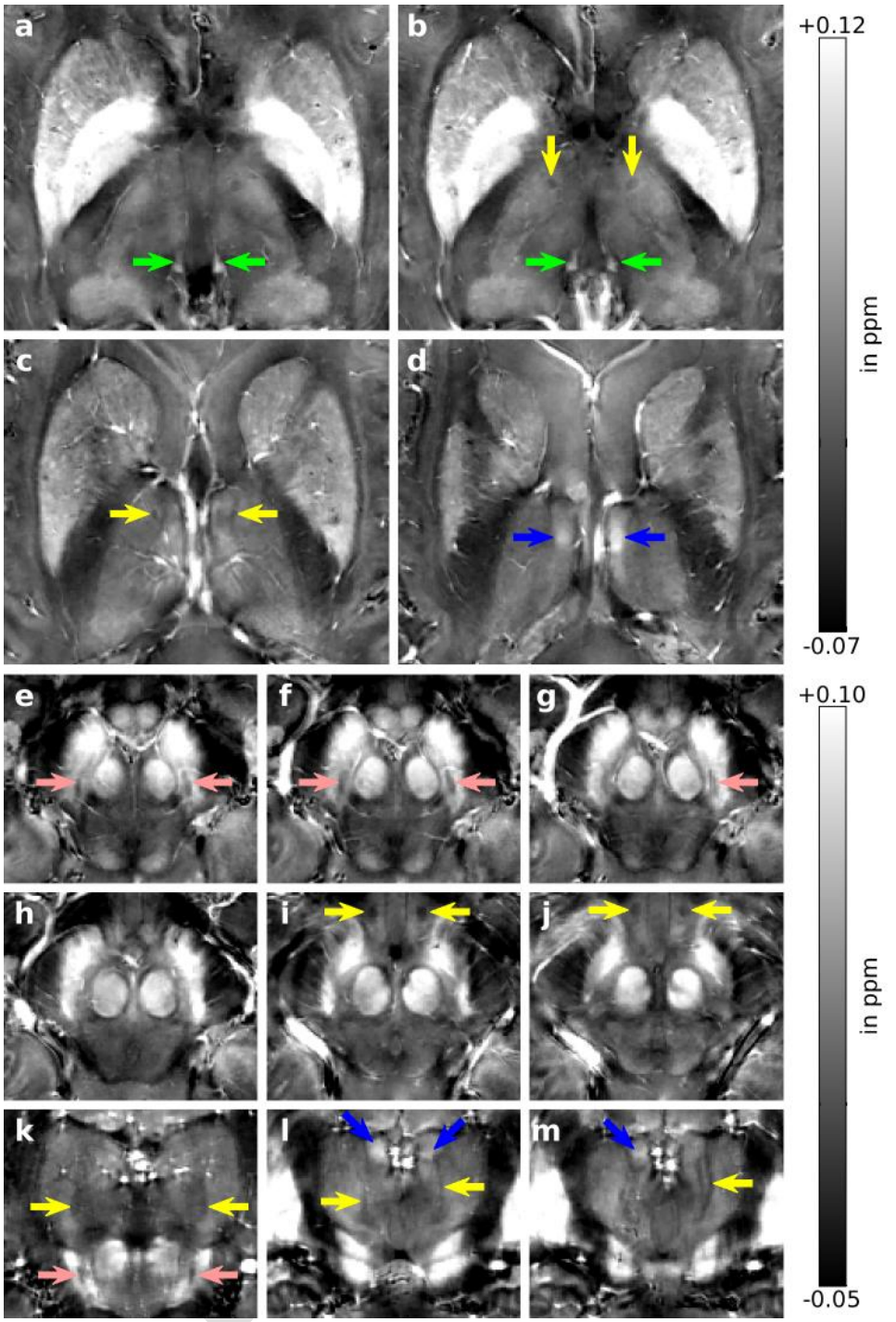

Figure 8: Magnified views of motion-corrected QSM at 0.33 mm isotropic voxel size: (a-d) axial views of corpus striatum/thalamus, (e-j) axial views of midbrain regions, and (k-m) coronal views of basal ganglia/thalamus (coronal). Arrows highlight the habenula (green), mammillothalamic tracts (yellow), anterior thalamic nuclei (blue), and substantia nigra nigrosome 1 (pink). QSM, Quantitative Susceptibility Mapping.

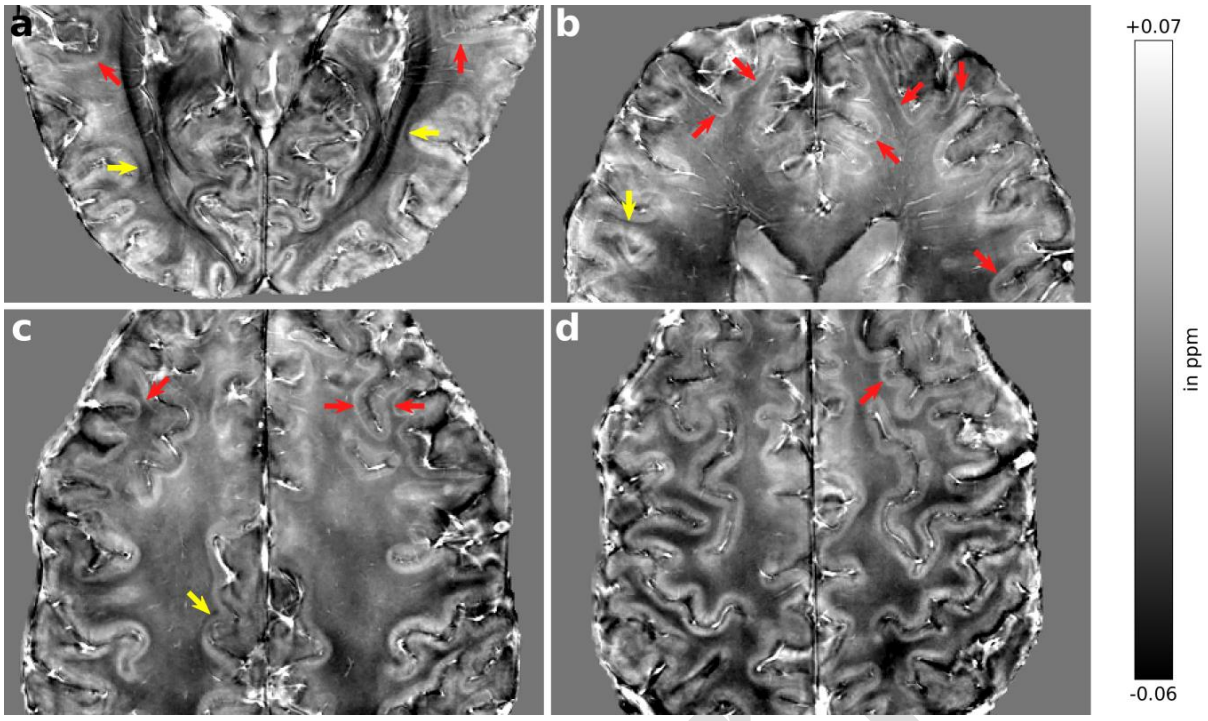

Figure 9: Magnified axial views of motion-corrected QSM at 0.33 mm isotropic voxel size across the cortex. Arrows highlight hypointense (yellow) and hyperintense (red) regions between gray matter and adjacent white matter.
QSM, Quantitative Susceptibility Mapping.

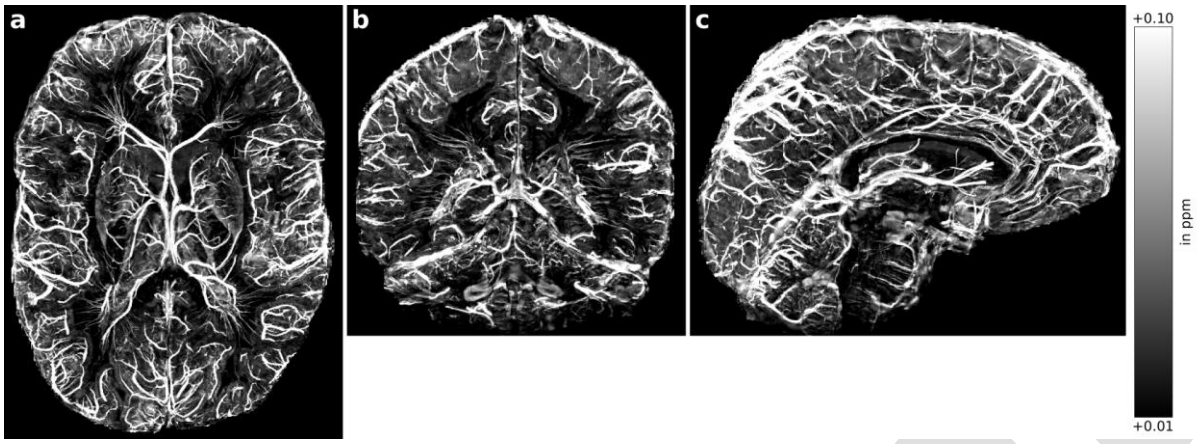

Figure 10: (a) Axial, (b) coronal, and (c) sagittal views of motion-corrected, QSM-based venogram at 0.33 mm isotropic voxel size. Hyperintense veins are enhanced by maximum intensity projection over 45 slices.
QSM, Quantitative Susceptibility Mapping.

Supporting Information

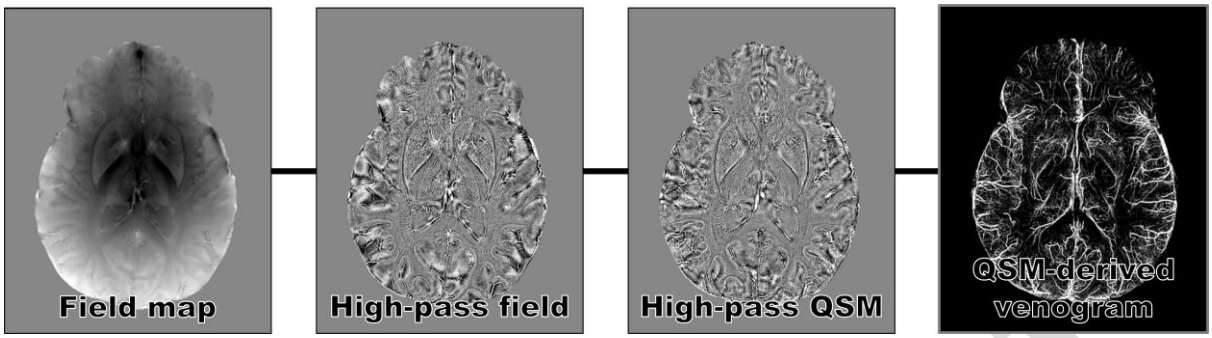

Supporting Information Figure S1: Illustration of the intermediate steps for QSM-based venogram estimation. The field map — computed as shown in Fig. 1 — was high-pass filtered to suppress low spatial frequencies, and was subsequently inverted with the nMEDI approach. After upsampling along the head-foot direction to improve vessel continuity, maximum QSM projections were computed, which revealed the hyperintense venous vasculature.
QSM, Quantitative Susceptibility Mapping.

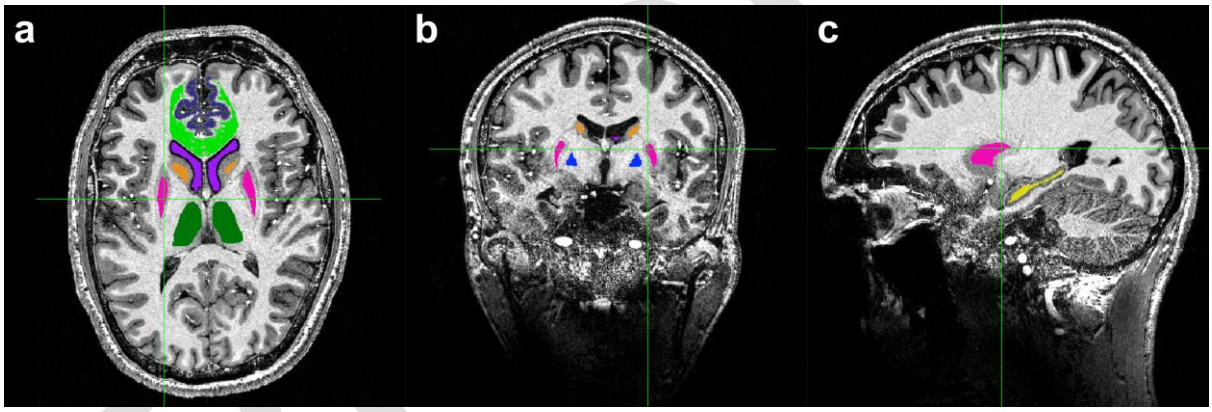

Supporting Information Figure S2: Regions of interest for regional susceptibility extraction overlaid onto an anatomical image: (a) axial, (b) coronal, and (c) sagittal views. ROIs: Globus pallidus (blue); caudate (orange); putamen (pink); thalamus (dark green); hippocampus (yellow); prefrontal gray matter (blue-gray); prefrontal white matter (light green); CSF (violet).

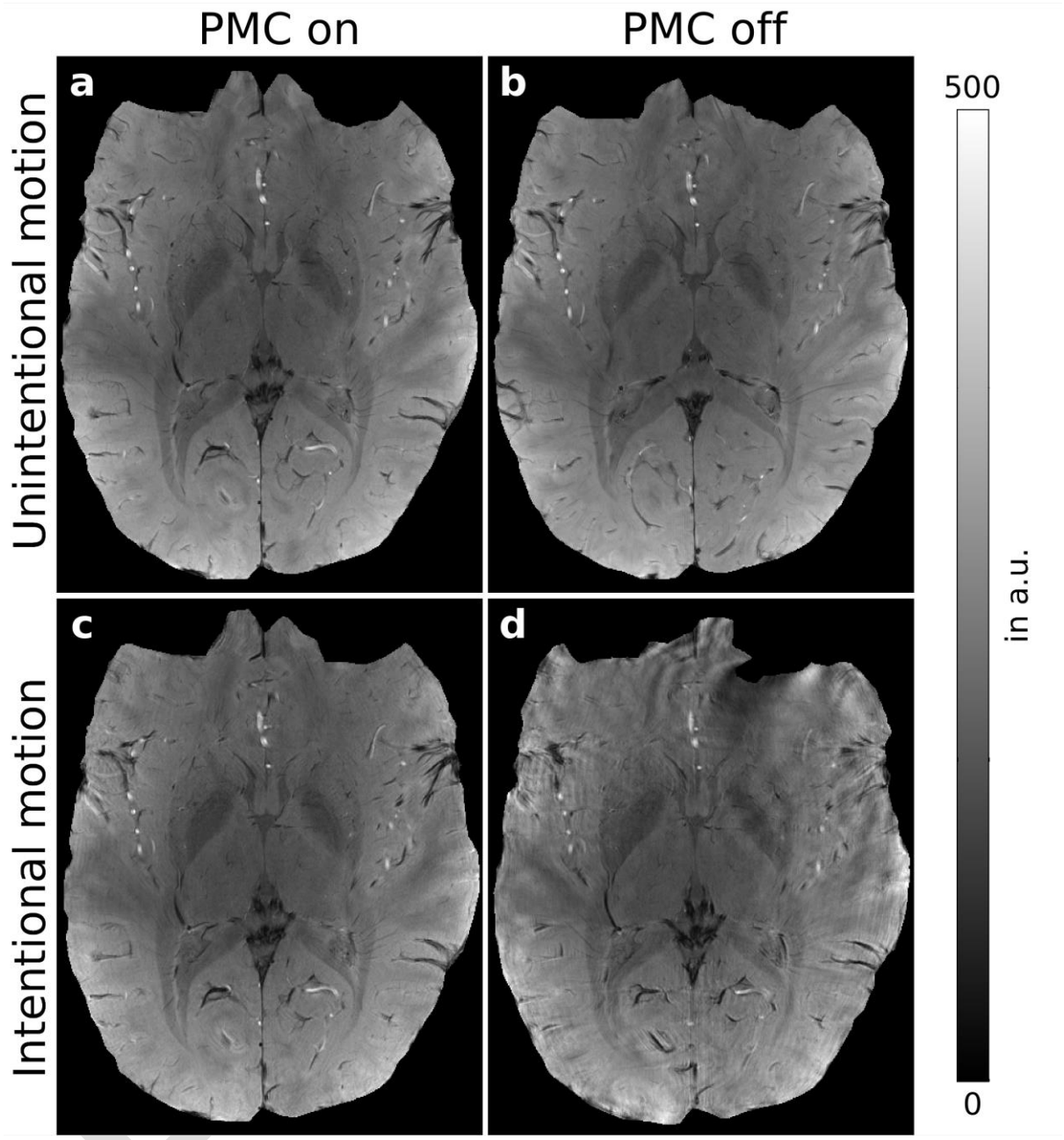

Supporting Information Figure S3: Intra-subject comparison (subject #3) of (a, c) motion corrected and (b, d) uncorrected magnitude images (after skull stripping) during (a, b) unintentional, small scale and (c, d) intentional, large-scale motion after brain extraction.

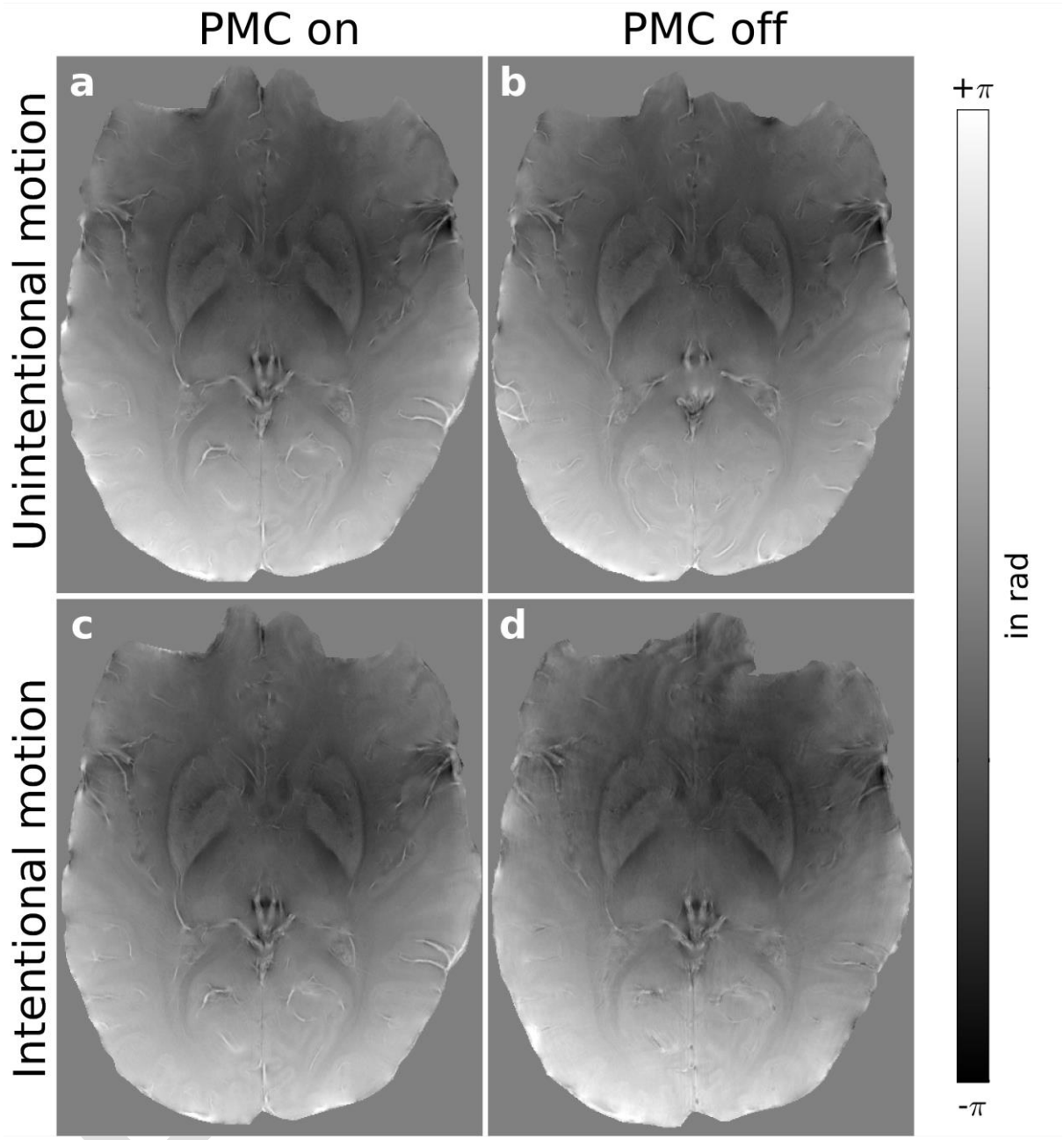

Supporting Information Figure S4: Intra-subject comparison (subject #3) of (a, c) motion corrected and (b, d) uncorrected field maps (unwrapped phase images) during (a, b) unintentional, small scale and (c, d) intentional, large-scale motion after brain extraction.

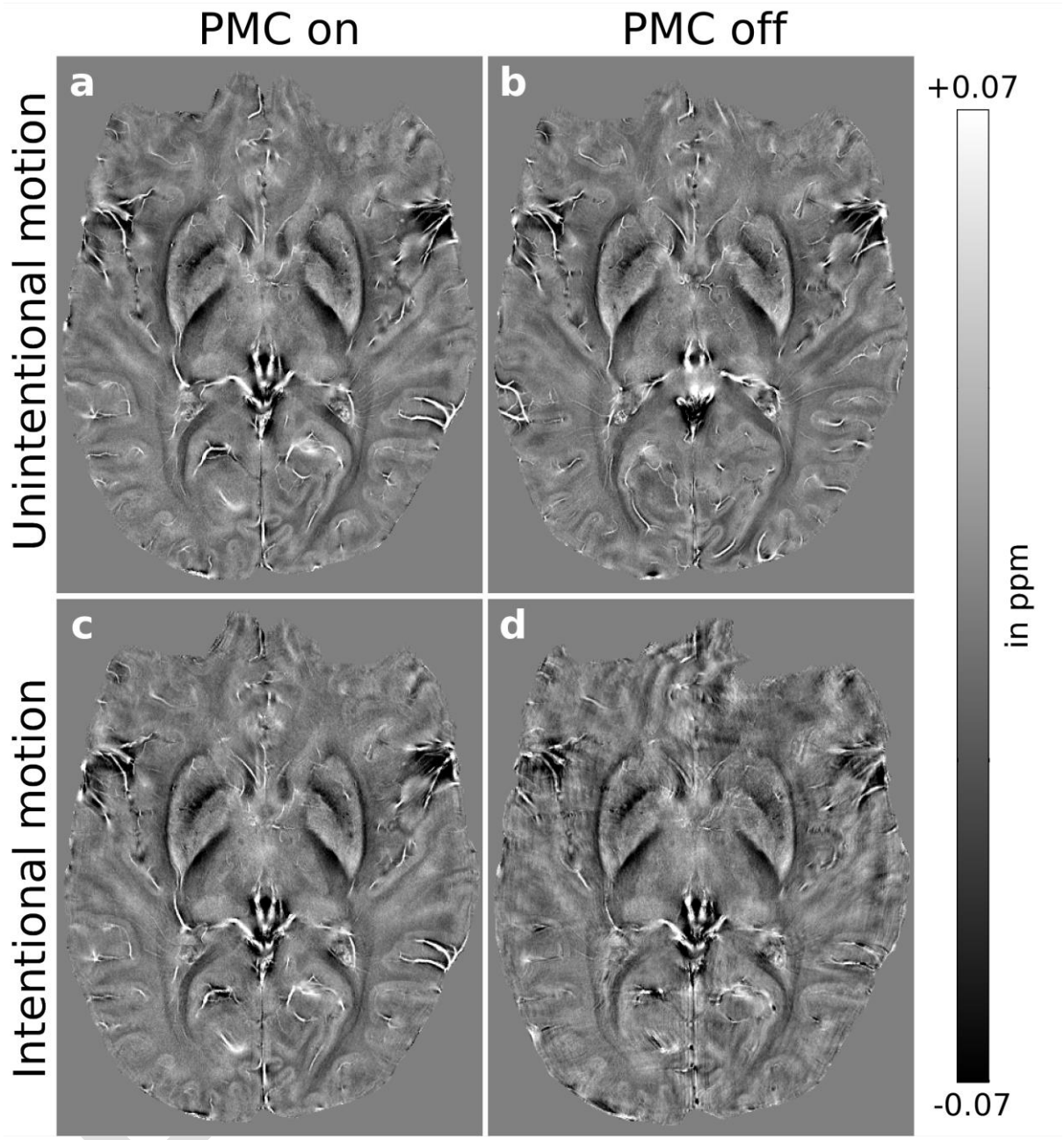

Supporting Information Figure S5: Intra-subject comparison (subject #3) of (a, c) motion corrected and (b, d) uncorrected local fields (SMV filtered) during (a, b) unintentional, small scale and (c, d) intentional, large-scale motion after brain extraction.
SMV, Spherical Mean Value.

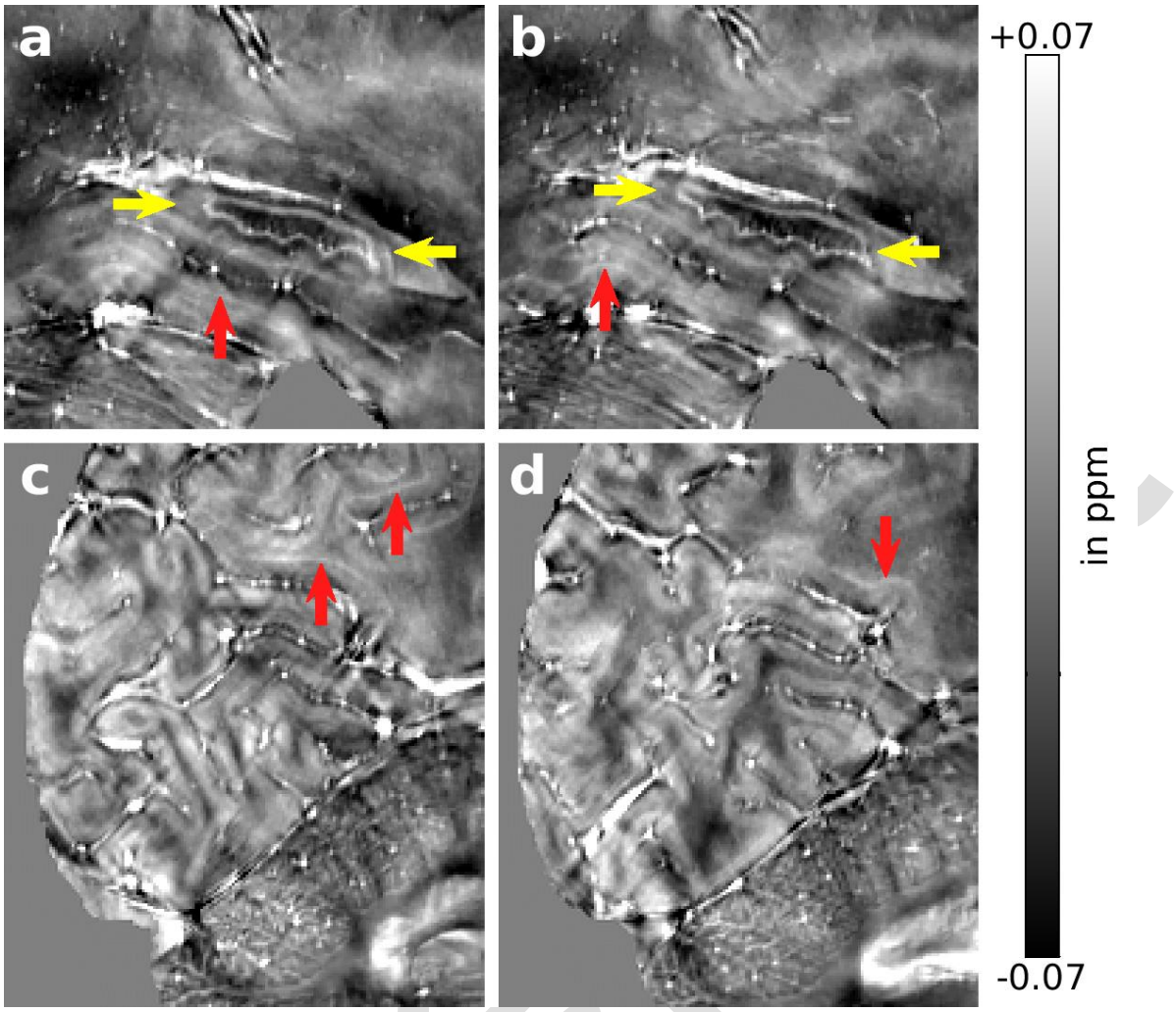

Supporting Information Figure S6: Magnified sagittal views of (a, b) the temporal lobe and (c, d) occipital lobe plus cerebellum for motion-corrected QSM at 0.33 mm isotropic voxel size. Red arrows highlight hyperintense regions between gray matter and adjacent white matter. Yellow arrows show hippocampus.
QSM, Quantitative susceptibility mapping.

Subject	Intentional Motion	PMC	Total Translation in [mm]	Total Rotation in [degrees]
1	No	On	0.49 ± 0.63	0.11 ± 0.18
1	No	Off	0.36 ± 0.26	0.12 ± 0.09
2	No	On	0.43 ± 0.12	0.21 ± 0.06
2	No	Off	1.19 ± 0.20	0.43 ± 0.08
3	No	On	2.19 ± 1.02	0.89 ± 0.42
3	No	Off	1.06 ± 0.22	0.45 ± 0.10
3	Yes	On	3.97 ± 2.03	1.31 ± 0.81
3	Yes	Off	1.93 ± 2.13	0.59 ± 0.83
4	No	On	1.47 ± 0.86	0.50 ± 0.29
4	No	Off	4.19 ± 1.59	0.68 ± 0.33

Supporting Information Table S1: Summary of motion quantification across subjects and scan types. Total translation and rotation denoting observed 3D movement during the whole scan are reported as mean ± standard deviation.
PMC Prospective Motion Correction

Subject	Intentional Motion	PMC	Pallidum	Caudate	Putamen	Thalamus	Hippocampus	Prefrontal GM	Prefrontal WM
1	No	On	0.098 ± 0.045	0.026 ± 0.031	0.022 ± 0.045	0.005 ± 0.033	-0.004 ± 0.044	0.002 ± 0.059	-0.001 ± 0.035
1	No	Off	0.088 ± 0.043	0.024 ± 0.032	0.019 ± 0.047	0.004 ± 0.032	-0.002 ± 0.043	-0.001 ± 0.057	0.001 ± 0.034
1	Yes	On	0.093 ± 0.042	0.029 ± 0.031	0.022 ± 0.047	0.007 ± 0.033	-0.004 ± 0.041	0.000 ± 0.056	0.002 ± 0.034
1	Yes	Off	0.094 ± 0.040	0.028 ± 0.035	0.016 ± 0.048	0.008 ± 0.035	-0.000 ± 0.045	-0.002 ± 0.064	0.001 ± 0.042
2	No	On	0.107 ± 0.067	0.032 ± 0.044	0.008 ± 0.041	0.004 ± 0.039	0.004 ± 0.031	-0.002 ± 0.043	0.003 ± 0.033
2	No	Off	0.105 ± 0.064	0.032 ± 0.041	0.010 ± 0.043	-0.001 ± 0.041	-0.002 ± 0.034	-0.000 ± 0.044	0.001 ± 0.032
3	No	On	0.119 ± 0.051	0.053 ± 0.027	0.024 ± 0.050	0.030 ± 0.046	0.012 ± 0.033	0.016 ± 0.054	0.021 ± 0.049
3	No	Off	0.117 ± 0.050	0.053 ± 0.026	0.026 ± 0.049	0.030 ± 0.046	0.010 ± 0.031	0.017 ± 0.053	0.021 ± 0.048
4	No	On	0.089 ± 0.043	0.030 ± 0.034	0.005 ± 0.041	0.005 ± 0.030	0.012 ± 0.028	-0.002 ± 0.060	0.005 ± 0.035
4	No	Off	0.095 ± 0.054	0.038 ± 0.035	0.013 ± 0.042	0.012 ± 0.033	0.010 ± 0.028	0.006 ± 0.058	0.010 ± 0.039

Supporting Information Table S2: Regional susceptibility values for all subjects summarized as mean ± standard deviation
PMC Prospective Motion Correction

Subject	PMC On vs. Off (regional mean QSM)		PMC On vs. Off (whole-brain QSM distributions, KS test statistic)
	P-value	signed rank	
1	0.81	12	0.003
2	0.38	20	0.008
3	0.16	23	0.007
4	0.03	1	0.019

Supporting Information Table S3: Statistics for motion-corrected versus uncorrected data (by subject). KS, Kolmogorov-Smirnov; QSM, Quantitative Susceptibility Mapping